

MADmap: A Massively Parallel Maximum-Likelihood Cosmic Microwave Background Map-Maker

C. M. Cantalupo

*Computational Cosmology Center, Lawrence Berkeley National Laboratory,
Berkeley, CA 94720, USA*

cmcantalupo@lbl.gov

J. D. Borrill

*Computational Cosmology Center, Lawrence Berkeley National Laboratory,
Berkeley, CA 94720, USA*

jdborrill@lbl.gov

A. H. Jaffe

*Department of Physics, Blackett Laboratory, Imperial College,
London SW7 2AZ, Great Britain*

a.jaffe@imperial.ac.uk

T. S. Kisner

*Computational Cosmology Center, Lawrence Berkeley National Laboratory,
Berkeley, CA 94720, USA*

tskinser@lbl.gov

R. Stompor

*CNRS, Laboratoire AstroParticule et Cosmologie, Université Paris-7 'Denis Diderot',
75205 Paris Cedex 13, France*

radek@apc.univ-paris-diderot.fr

ABSTRACT

MADmap is a software application used to produce maximum-likelihood images of the sky from time-ordered data which include correlated noise, such as those gathered by Cosmic Microwave Background (CMB) experiments. It works efficiently on platforms ranging from small workstations to the most massively parallel supercomputers. Map-making is a critical step in the analysis of all CMB data sets, and the maximum-likelihood approach is the most accurate and widely applicable algorithm; however, it is a computationally challenging task. This challenge will only increase with the next generation of ground-based, balloon-borne and satellite CMB polarization experiments. The faintness of the B-mode signal that these experiments seek to measure requires them to gather enormous data sets. MADmap is already being run on up to $O(10^{11})$ time samples, $O(10^8)$ pixels and $O(10^4)$ cores, with ongoing work to scale to the next generation of data sets and supercomputers. We describe MADmap's algorithm based around a preconditioned conjugate gradient solver, fast Fourier transforms and sparse matrix operations. We highlight MADmap's ability to address problems typically encountered in the analysis of realistic CMB data sets and describe its application to simulations of the Planck and EBEX experiments. The massively parallel and distributed implementation is detailed and scaling complexities are given for the resources required. MADmap is capable of analysing the largest data sets now being collected on computing resources currently available, and we argue that, given Moore's Law, MADmap will be capable of reducing the most massive projected data sets.

Subject headings: Cosmic Microwave Background, data analysis, map making, maximum likelihood

1. Introduction

The Cosmic Microwave Background (CMB) is the left-over radiation from the Big Bang. This radiation is comprised of primordial photons last scattered when the first neutral atoms formed some 400,000 years after the Big Bang. The subsequent expansion of the Universe redshifts the spectrum of these photons, originally distributed as a 3000K black body, to appear in contemporary observations as a 3K black body. Encoded within the image of the thermal fluctuations in the CMB are not only the signatures of the basic parameters of cosmology but also, using the Big Bang as the ultimate particle accelerator, insights into fundamental physics at the very highest energies (Dodelson 2003).

Most CMB experiments simply scan across the sky, sampling its temperature (and now polarization) at one or more microwave frequencies at some fixed rate. Once these data have been cleaned and calibrated, the first step in their scientific analysis involves producing pixelized maps of the sky and at least an estimate of the pixel noise properties. Subsequent steps include separating these sky maps into distinct CMB and foreground component maps, estimating the power spectra of the CMB from its maps, and estimating cosmological parameters from these power spectra. Since these subsequent steps depend on the quality of the original maps, it is important to generate the most accurate and well-characterised maps we can, in particular maximum-likelihood, minimum variance maps. However, the faintness of the CMB fluctuations on the sky drives us to gather enormous data sets which must be reduced coherently if we are to preserve their scientific content, resulting in a very significant computational challenge.

The computational costs of the dominant CMB analysis steps (in floating-point operations, memory, communication, and input/output) are set by the numbers of time samples n_t and sky pixels n_z . As the goals of CMB experiments have evolved, both of these numbers have grown. The growth in the number of samples is driven by the quest for fainter polarized and high multipole signals, and the number of pixels is driven by the sky-coverage and resolution required for measuring low and high multipole signals respectively. Table (1) shows this evolution for a representative selection of sub-

orbital and all anticipated satellite CMB missions.

Since brute force dense matrix maximum-likelihood algorithms scale as $O(n_z^3)$ (Borrill 1999) they have become computationally intractable, and we have had to adopt alternative approximate algorithms that are dominated by operations on the time-ordered data that are linear and log-linear in n_t . Over the next 15 years we can expect CMB time-ordered data volumes to grow by 3 orders of magnitude; coincidentally this exactly matches the projected growth in computing power over the same period assuming a continuation of Moore's Law. Since CMB data analysis is already pushing the limits of current state-of-the-art HPC systems, this implies that our algorithms and implementations will have to continue scaling on the leading edge of HPC technology for the next 10 Moore-doublings if we are to be able fully to support first the design and deployment of these missions and then the scientific exploitation of the data sets they gather.

The next section gives an overview of the computational context for the MADmap software: the libraries it depends on, the supporting applications, and hardware platforms targeted. Section 3 describes the formalism which is applied to the data by MADmap including the statistical derivation and mathematical framework. MADmap is designed around the method of preconditioned conjugate gradients, and Section 4 describes this algorithm. Section 5 details MADmap's implementation, including subsections on data distribution, noise weighting, pointing data compression, pixel indexing, and the functional complexity of the communication, memory, CPU and disk requirements of MADmap. Section 6 explores the versatility of the MADmap data model, and describes a variety of real world problems that MADmap has been used to solve. Section 7 describes a set of MADmap runs on simulated Planck and EBEX data and explains in detail the performance characteristics of these runs which span a range of data sizes in both the time and pixel domain and a variety of processor counts. The paper finishes with a comparison with other software, a discussion of future work, and concluding remarks.

We will use the following notation in this paper: variables in unitalicized roman font are scalars (e.g., n_t and n_i), time domain vectors are represented by italic Greek letters (e.g., γ and ν), pixel

Date	Experiment	Description	Samples (n_t)	Pixels (n_z)
1990-93	COBE	All-sky, low-res, T	8×10^8	3×10^3
1998	BOOMERanG	Cut-sky, mid-res, T	9×10^8	3×10^5
2001-10	WMAP	All-sky, mid-res, TE	2×10^{11}	6×10^6
2009-11	Planck	All-sky, high-res, TE	3×10^{11}	1×10^8
2010	EBEX	Cut-sky, high-res, TEB	3×10^{11}	6×10^5
2010-12	PolarBeaR	Cut-sky, high-res, TEB	3×10^{13}	1×10^7
2010-13	QUIET-II	Cut-sky, high-res, TEB	1×10^{14}	7×10^5
2020+	CMBpol	All-sky, high-res, TEB	1×10^{15}	9×10^8

Table 1: The evolution of sample and pixel counts over time for a representative selection of suborbital and all anticipated satellite missions. Details of the proposed CMBpol satellite are from the EPIC Intermediate Mission concept study. To allow meaningful comparison, the *effective* number of samples and pixels for each experiment are given, which may differ from those quoted by the respective experiment teams. Specifically, sample counts are defined as the sum over all of an experiment’s time-ordered data streams of the stream’s sampling rate times the duration of its observation (where data streams may include various combinations of detector streams), while pixel counts are the sum over all observing frequencies of the fraction of the sky observed divided by the fiducial beam size, assuming a circular beam with diameter given by the assumed full-width at half-maximum, at that frequency.

domain vectors are represented by italic Roman letters (e.g., y and z), and matrices are capitalized (e.g., A and B).

2. MADmap

Under the assumption of piecewise stationary Gaussian noise (defined more precisely below) with known spectral properties MADmap produces maximum-likelihood maps to user-specified precision, and in particular does so for the very largest real and simulated CMB data sets extant and on the very largest of today’s supercomputers. For example, MADmap can enable a wall-clock time to solution of tens of minutes for Planck-like data volumes running on a significant fraction of the 40,000-core Cray XT4 at the US Department of Energy’s National Energy Research Scientific Computing Center. Supercomputers will be a crucial resource in the analysis of forthcoming CMB data sets and MADmap’s ability to scale to use large computing resources will enable science that would be otherwise inaccessible (Bock et al. 2006). The maps’ noise properties can be calculated by other tools in the MADCAP software suite. MADpre, an application distributed with MADmap, generates the auto-correlation matrix assuming time domain white noise (which can be used as a preconditioner by MADmap), while MADping calculates the full dense noise covari-

ance matrix by explicit inversion, although this is impractical for more than $O(10^5)$ pixels.

These software components take advantage of a set of libraries to facilitate simulation and input/output operations. M3 is a data abstraction library that uses a plug-in architecture to enable analysis applications to ingest data from a variety of experiments, which invariably adopt different data formats and distributions. Crucially, M3 can also simulate simple signals and complex noise on the fly, which reduces the potentially overwhelming I/O and disk cost of the traditionally separate simulation and analysis steps. Similarly, the Generalized Compressed Pointing (GCP) library, described in more detail below, has been devised to calculate the pointings of individual detector samples on demand at run time from compressed pointing information (e.g., the sparse-sampled pointing of a reference frame, such as the focal-plane bore-sight).

MADmap was originally designed to map CMB data in a manner independent of any individual CMB experiment, and has been applied to real and simulated data from a number of missions including the historic BOOMERanG (de Bernardis et al. 2000) and MAXIMA (Hanany et al. 2000) experiments, and the upcoming EBEX¹ (Oxley

¹EBEX: <http://groups.physics.umn.edu/cosmology/ebex/>

et al. 2004) balloon and Planck² satellite missions. However the problem it solves appears in any situation where a signal described by a sparse linear model is to be derived from data containing correlated Gaussian noise that is stationary over known intervals, and it is already being used in other domains, for example by the Herschel mission (Waskett et al. 2007).

We also note that map-making-like operations are commonly used in other stages of the data analysis, including power spectrum estimation via sampling algorithms (Jewell et al. 2004; Wandelt et al. 2004) and component separation via parametric technique (Stompor et al. 2009), and MADmap can be employed in a straightforward manner in all those contexts.

3. Formalism

The central assumption of our map-making is that the time-ordered data measured by each detector, γ , can be written

$$\gamma = \nu + \zeta \quad (1)$$

$$\zeta = Az \quad (2)$$

for temporal noise ν , pixelized signal z , and a sparse pointing matrix A encoding the weights with which each pixel is observed at each time. In the simplest case (a total power CMB temperature with uniform symmetric beams in the limit of small pixels compared to the beam size) the pointing matrix contains a single unit weight per observation; at time sample t with the detector pointed at sky-coordinates (θ_t, ψ_t)

$$A_{t,p} = \begin{cases} 1, & \text{if } (\theta_t, \psi_t) \in \text{pixel } p; \\ 0, & \text{otherwise.} \end{cases} \quad (3)$$

For ideal polarization experiments, this single weight is then replaced by one for each of the Stokes parameters in the observed pixel:

$$\zeta_t = \frac{1}{2} [i_p + q_p \sin(2\alpha_t) + u_p \cos(2\alpha_t)] \quad (4)$$

where α is a time ordered vector of the observed polarization angle, and we consider the signal as a vector $z = [i, q, u]$. More complex beams may

be incorporated by appropriately weighting multiple pixels in each observation, and parasitic signals that are fixed in any other basis (for example, MAXIMA's chop-synchronous signal (Stompor et al. 2002)) can be simultaneously solved for by extending the pixel basis appropriately (see also Section 6). Ultimately the only requirement on A is that it be full rank, which is to say that there are at least as many linearly independent observations as there are signals that are being solved for. In the broadest sense the pointing matrix is a projection from the signal basis to the time basis that defines the linear relationship between the signal to be solved for and the recorded detector time stream.

Representing now the noise as,

$$\nu = \gamma - Az \quad (5)$$

and making use of its Gaussian properties we can write the likelihood function of a pixelized sky map z given our data γ as

$$\mathcal{L}(z|\gamma) \propto \exp \left\{ -\frac{1}{2} (\nu^T N^{-1} \nu + \text{Tr} [\ln N]) \right\}, \quad (6)$$

where we have used the matrix identity

$$\text{Tr} \ln H = \ln \det H \quad (7)$$

to move the usual Gaussian prefactor into the exponential. Maximizing this over all *a priori* equally likely signals z , gives the maximum-likelihood map and its noise correlation matrix

$$\begin{aligned} \hat{z} &= MA^T N^{-1} \gamma \\ M &= (A^T N^{-1} A)^{-1} \end{aligned} \quad (8)$$

which can also be derived as the minimum variance or generalized least squares solution (de Gasperis et al. 2005). In addition, the map \hat{z} is a sufficient statistic for the likelihood functions as written. That is, the Gaussian likelihood of a sky map z only depends on the estimate \hat{z} and no other function of the data:

$$\mathcal{L}(z|\hat{z}) \propto \exp \left\{ -\frac{1}{2} [(z - \hat{z})^T M^{-1} (z - \hat{z}) + \text{Tr}(\ln M)] \right\} \quad (9)$$

where the map noise correlation matrix is M .

These equations reduce to simple averaging into pixels in the white noise limit, $N_{t,t'} = \sigma^2 \delta_{t,t'}$. We

²Planck: http://www.esa.int/esaSC/120398_index.0.m.html

note that the $O(n_z^3)$ scaling of the brute force explicit dense matrix calculation arises from the inversion of the inverse pixel noise matrix, although it is important to note that the computational cost of building the matrix before inversion, $O(n_t n_c)$, may dominate $O(n_z^3)$ for some experiments.

Our solution \hat{z} is only the maximum-likelihood estimate of z only if N is the true noise correlation matrix, and since the noise properties of CMB data have to be derived from the data there will inevitably be uncertainties. However, provided N is positive definite, then \hat{z} provides an unbiased, though potentially not optimal, estimate of z .

4. Algorithm

Brute force explicit dense matrix computation of Equation (8), requiring the construction and inversion of the full dense pixel-pixel noise correlation matrix, is computationally impractical for current and future CMB data sets with millions to hundreds of millions of pixels. However, we observe that it can be re-written in standard linear form (Oh et al. 1999),

$$Hx = b \quad (10)$$

where $H \equiv A^T N^{-1} A$, $b \equiv A^T N^{-1} d$ and $x \equiv \hat{z}$.

Since N^{-1} is positive definite (being a correlation matrix) and A is full rank (by assumption, but see the discussion later in this section), H is also guaranteed to be positive definite. Now provided we can operate on any time-domain vector with N^{-1} (weighting) and A^T (pointing), and on any pixel-domain vector with A (unpointing), we can solve for x using preconditioned conjugate gradient (PCG) - a widely-used technique for solving positive definite linear systems that provides the fastest time to solution for many problems (especially sparse systems), (Barrett et al. 1994; Shewchuk 1994).

The method of conjugate gradients is an optimization algorithm similar to steepest decent except that search directions are chosen to be orthogonal to each other. This optimization is applied to minimize the quadratic form:

$$g(x) = \frac{1}{2} x^T H x - b^T x + c \quad (11)$$

which has the following derivative with respect to x :

$$g'(x) = Hx - b. \quad (12)$$

When H is positive definite g is a convex quadratic, so that when the gradient of g is zero we have both minimized g and solved the original linear system of Equation (10). Embedding the solution of a positive definite linear system into the optimization of a convex quadratic may at first seem just to complicate matters, but operationally it buys us a lot if we can operate with H on a vector quickly and with minimal memory overhead. This is an iterative technique, and each iteration involves the operation of H on a vector, which is the dominant computational cost of the algorithm. Since the number of iterations required to converge to the solution is proportional to the condition number of H , having an approximate inverse of H that can multiply a vector quickly can greatly reduce the number of iterations required by making the effective matrix in the preconditioned system approximate the identity matrix.

The time streams collected by CMB telescopes generally contain large low frequency correlations in the noise which is often referred to as “1/f-noise”. The noise power spectrum [the Fourier transform of the noise correlation function $n(|t - t'|)$] can be modelled as

$$p(f) = \sigma^2 [1 + (f_k/f)^\alpha] \quad (13)$$

with a white noise level σ , knee-frequency f_k , and typically power law $1 \leq \alpha \leq 2$. Having power inversely proportional to frequency clearly blows up for the constant mode ($f = 0$)³. This (near) degeneracy produces a null space to the constant mode in the inverse pixel pixel noise correlation matrix, and therefore the inverse problem is ill-posed (equivalently, the H matrix is only positive *semi*-definite). Applying the conjugate gradient technique to such ill-posed problems has been discussed in the literature (Brakhage 1996), and used in many fields. In the specific example discussed here, the total offset of the estimated map is arbitrary. In a more general case such degeneracies may result from the presence of (or removal of) a systematic effect in the time-ordered data, and need to be considered case by case. In general when applying conjugate gradient to semi-definite linear systems the iterates will begin by converg-

³We note that for real detectors the power at zero frequency is clearly finite, though still high enough to lead to a numerical near degeneracy.

ing toward the optimal solution until a point after which subsequent iterations begin to diverge from the solution. Choosing when to stop iterating is the key to dealing with ill-posed problems, and this is discussed in more detail in Brakhage (1996).

Observations of CMB polarization can also introduce degeneracies if a particular pixel is not observed with sufficiently many different orientations to separate the 3 Stokes parameters. This situation can be resolved by identifying such pixels ahead of time (for example by examining the conditioning of the 3×3 blocks, or an appropriate generalization of those if different pixel resolutions are adopted for different Stokes parameters, in the $A^T A$ matrix) and excising poorly-conditioned pixels.

Removing pixels from the map and therefore their respective samples from the time stream affects the structure of the time-domain noise correlation matrix, making it non-Toeplitz, and thus difficult to handle efficiently, whenever the noise is correlated. This problem can be overcome by the so-called gap filling procedure Stompor et al. (2002), which within the MADCAP software suite can be facilitated by the MADmask and MADnes applications. These tools replace time ordered data samples that occur while an excised pixel is observed by simulated noise that is consistent with the power spectrum associated with each excised sample and the correlations inferred by the noise in surrounding samples. In this way the continuity and stationarity of the time-domain noise is preserved, together with the Toeplitz character of its respective noise correlation matrix. The rows of the pointing matrix that correspond to observations of excised pixels are set to zero, and this models the simulated noise as free of signal.

5. Implementation

The core of MADmap is a massively parallel implementation of a preconditioned conjugate gradient (PCG) solver. Each PCG iteration moves in a direction in the solution space that is orthogonal to all previous steps. In the absence of numerical error and degeneracies in the system the exact solution is guaranteed after n_z steps because the number of possible directions has been exhausted. In practice however the calculation is

terminated either after a fixed number of iterations n_i , or after achieving a given accuracy as measured by the relative residual ϵ (in the absence of user-specified values MADmap defaults to $n_i = 50$, $\epsilon = 10^{-6}$). On termination MADmap outputs the vector which produced the lowest relative residual thus far, which is not necessarily the last iteration of the PCG as the relative residual is not guaranteed to decrease monotonically with iterations. By algorithmic design the relative error does not increase with iteration.

It is possible to precalculate a sparse preconditioner and have MADmap read this preconditioner in from disk at run time; for example, the MADpre code will precompute and store $(A^T W^{-1} A)^{-1}$, where W^{-1} is simply N^{-1} with all off-diagonal elements set to zero. This is the noise correlation matrix if white noise is assumed in the time domain. If no preconditioner file is specified then by default MADmap calculates the point Jacobi preconditioner which is the diagonal matrix composed of the inverse of the diagonal elements of $A^T A$.

To minimize the impact of system failure on a calculation in progress, MADmap checkpoints periodically and can restart from any of these. By default MADmap checkpoints every 20 PCG iterations, although this can be altered by setting an environment variable⁴. Each checkpoint comprises five map vectors and six scalars, with the distributed maps being gathered onto the root processor before being written to disk. At a checkpoint restart this process is inverted, and the root processor reads the maps (and scalars) from disk and scatters them to the other processors. In this way the checkpoint data volume and distribution is independent of the number of processors used, and a restarted job is not required to use the same number of processors as the original. Figure 1 is an overview of the map making process.

5.1. Data Distribution

The memory for both the time domain data and the pixel domain data are distributed over processors. The user has options regarding how the time domain data will be distributed in ways that allow for CPU and memory resource opti-

⁴The checkpoint frequency environment variable: `MM_CHECKPOINT_FREQUENCY`

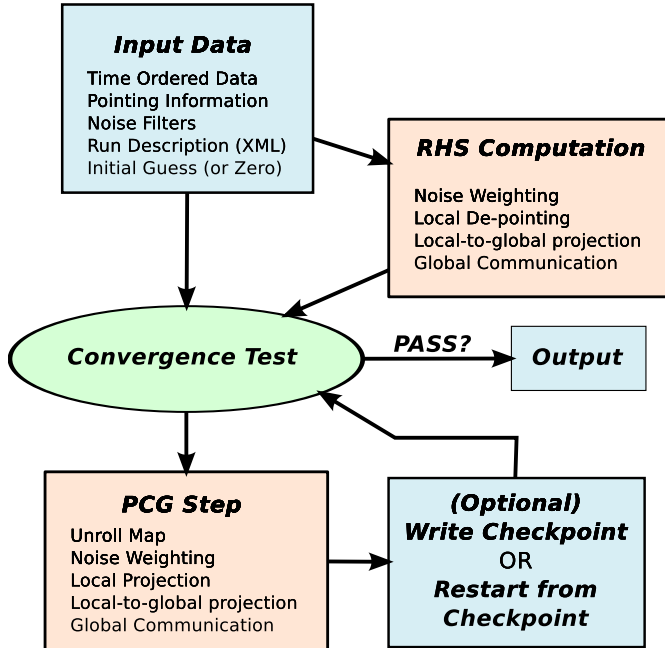


Fig. 1.— A graphical overview of MADmap. Blue boxes represent data products and pink boxes represent computational procedures, where RHS is the “right hand side” calculation.

mization depending on the details of the problem being solved and the architecture of the available hardware. MADmap has several options that allow the user to tune the total memory consumption in compromises between memory and CPU resources.

MADmap uses the MPI library to enable the use of distributed parallel computing resources. MPI uses a single program multiple data parallel model. The computational load scales with the number of time samples assigned to each processor. In order to load balance computation we attempt to load balance total sample count. There are three memory modes in which MADmap can be run. In the high memory mode, the full detector pointing is held in memory concurrently. The other data objects which are required in high memory mode are the noise filters. In low memory mode, the compressed telescope pointing and the noise filters are the only persistent time domain data objects. In very low memory mode, only the compressed telescope pointing remains in memory and the memory requirement is independent of the detector count.

MADmap distributes its data by dividing the time stream data over the processors. Then the pixels are distributed so that each processor stores the pixels observed in the sections of the detector time streams that are assigned to it. MADmap is enabled to use three different data distributions: concatenated mode, stacked mode, and multi-stacked mode. In the concatenated distribution each detector time stream is concatenated with all the others and the resulting “super” time stream is evenly divided among the processors. In the stacked distribution each processor analyzes data from all detectors, and the experiment’s run time is divided evenly over the processors. The multi-stacked distribution is a compromise between the other two, and provides the option to stride the detectors over the processors. That is to say that if the stride was s , then each processor would analyze the data from the fraction $1/s$ of the detectors, and the experiment’s run time is evenly divided among processors who have a common remainder when divided by s .

Figure 2 is a graphical representation of the memory distribution for the detector time streams

and telescope pointing. Figure 3 shows a toy mapping of each processors’ locally observed pixels to the global pixel space. The pixel data that is stored in the memory of each processor corresponds to those pixels which were observed by the detector samples within the time streams analyzed by the processor. This means that the distribution of the pixel data is strongly dependent on the scanning strategy of the experiment and the relative locations of the detectors on the focal plane in addition to the effects of the different modes of time stream distribution and the number of processors used to analyze the data.

The concatenated distribution has several advantages over the unstrided stacked mode, but there are some very critical advantages to the stacked mode that make it quite useful. The multi-stacked distribution is often a good compromise that will allow the problem to be tackled with the computational tools available given a good choice of stride. In the unstrided stacked mode all of the the detector-specific noise filters are required to be stored on each processor, compared with very few in the concatenated mode. The concatenated distribution can be used to simultaneously analyze data from different experiments, or data sets that have large gaps in time where no data are taken. In the case of run time simulation of correlated noise, the concatenated mode allows for load balanced generation of correlated noise for longer intervals of time on a each processor than in the unstrided stacked mode. In this case the use of the concatenated mode provides the ability to scale this calculation to larger numbers of processors. The unstrided stacked distribution is advantageous because this is optimal for the storage and computational requirements of expanding the compressed pointing data that is shared by all the detectors for each time sample.

5.2. Weighting

If the instrumental noise is a least piece-wise stationary, N will be a block-diagonal Toeplitz matrix, with each block corresponding to one of the stationary pieces. A Toeplitz matrix is defined so that each row is shifted by one entry from the one above. For an $n \times n$ Toeplitz matrix,

$$T_{i,j} = T_{i-1,j-1} \quad \forall i \ \& \ j \in \{1, \dots, n-1\}. \quad (14)$$

Moreover, for a typical experiment each of the diagonal blocks will be banded. Generally, the inverse of a Toeplitz matrix is not Toeplitz, however for banded matrices this is nearly true with potential departures seen only at the first and last rows and columns of the diagonal block (Stompore et al. 2002). Moreover, the inverse of a banded-matrix is also, to a good approximation, banded with a band-width which needs to be appropriately tuned. The MADmap algorithm assumes therefore that N^{-1} is a block-diagonal, banded Toeplitz matrix.

$$N_{t,t'}^{-1} = \begin{cases} f(|t-t'|) & \text{if } |t-t'| < n_c \\ 0 & \text{otherwise} \end{cases} \quad (15)$$

We note that though it is a very good approximation, it is still an approximation; however, at worst it can only compromise the optimality of the MADmap map without biasing it.

The method used by MADmap for convolution with a filter is similar the the “overlap and add method” outlined in Numerical Recipes (Press et al. 1992). The method given here is slightly different and requires fewer computations by avoiding two correlation length additions for each FFT computed. The method presented also gives an algorithm for choosing the FFT length which is optimal in terms of number of operations required.

The discrete Fourier transform operator diagonalizes circulant matrices, and it is well known that the fast Fourier transform algorithm of Cooley and Tukey (Cooley & Tukey 1965) can be used to quickly compute the action of a circulant matrix on a vector. This algorithm has a computational complexity of $O(n_f \log(n_f))$, where n_f is the length of the vector and size of the matrix. A circulant matrix is a special type of Toeplitz matrix with the additional constraint of periodic boundary conditions (e.g., Golub & van Loan 1996):

$$C_{i,j} = C_{i-1,j-1} \quad \forall i \ \& \ j \in \{1, \dots, n-1\} \quad (16)$$

$$C_{0,j} = C_{n-1,j-1} \quad \forall j \in \{1, \dots, n-1\} \quad (17)$$

$$C_{i,0} = C_{i-1,n-1} \quad \forall i \in \{1, \dots, n-1\} \quad (18)$$

The inverse time-time noise correlation matrix, N^{-1} is block diagonal and these blocks are themselves band diagonal and Toeplitz. Our objective is to use circulant matrix multiplies as a building block from which we can compute the action of N^{-1} . We can treat each diagonal block of N^{-1}

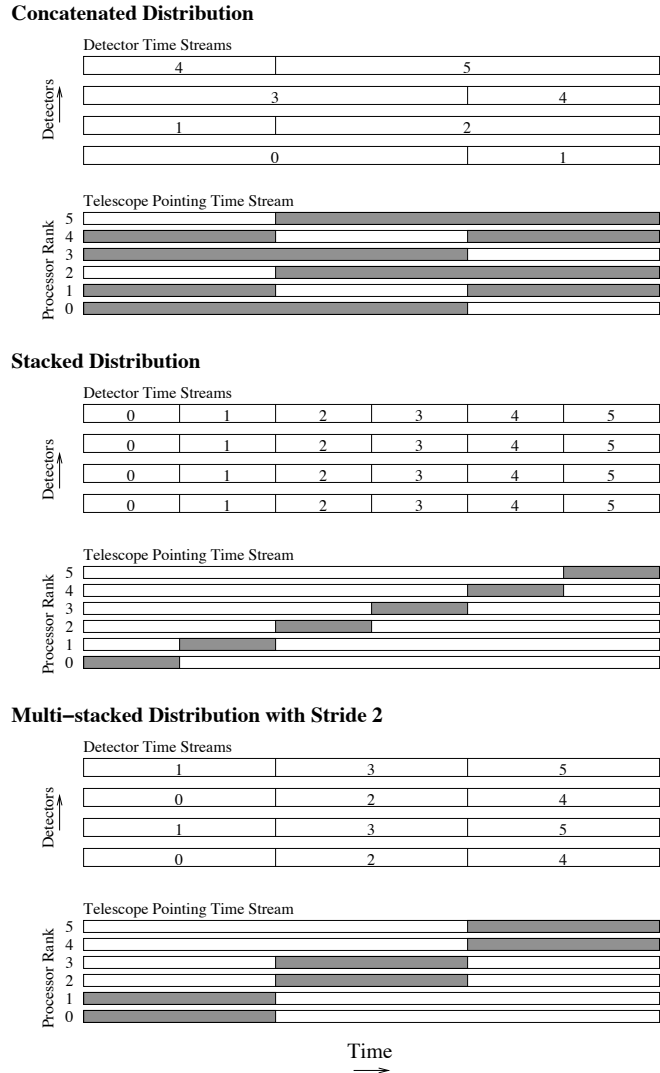


Fig. 2.— This is a graphical representation of the data distribution for the detector time streams and the telescope pointing time stream. The cartoon represents the distribution of four detector time streams over six processors in the three different modes of operation. The numbers labeling the figure all represent processor ranks. Note that the detector time streams are distributed over the processors, where as the telescope pointing is only fully distributed in the stacked mode. For this reason we can show the distribution of the detector time streams over all of the processors in one image but the telescope pointing data distribution must be shown for each processor individually where gray indicates telescope pointing that is stored on a given processor.

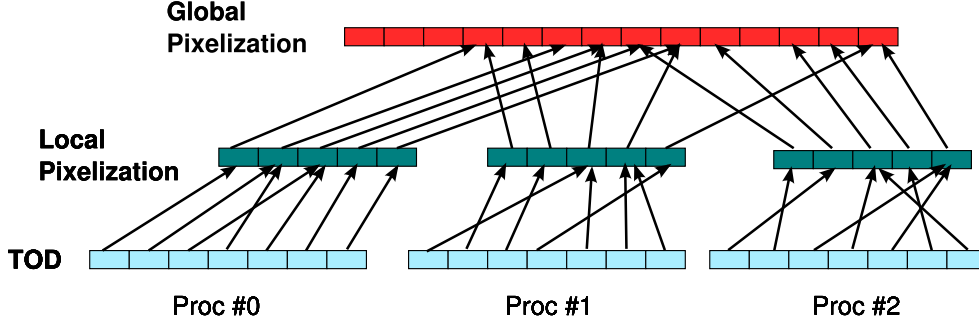


Fig. 3.— This is a graphical representation of the distribution of pixel domain data between processors. Each processor has a set of time samples and the minimal set of “local pixels” needed for the pointing in those samples. These local pixels have a further mapping to global pixels on the sphere.

as an independent problem, so let us simply consider the problem of multiplying a band diagonal Toeplitz matrix with a bandwidth of n_c where

$$B_{i,j} = B_{i-1,j-1} \quad \forall i \ \& \ j \in \{1, \dots, n_c\} \quad (19)$$

$$B_{i,j} = 0 \quad \forall i \ \& \ j \text{ s.t. } |i - j| > n_c \quad (20)$$

We can approximate B with a circulant matrix C which differs from B only in the upper right and lower left corners of the matrix

$$B_{i,j} = C_{i+b,j+b} \quad \forall i \ \& \ j \text{ s.t. } |i - j| < n - n_c \quad (21)$$

In order to compute the action of B on a vector by using a circulant matrix C , we construct C to be two bandwidths larger than B and pad the vector to be multiplied with a bandwidth of zeros at the beginning and end. The vector that results from the multiplication of C by the zero-padded vector will be the correct solution to the original problem once a bandwidth has been trimmed from the beginning and end of the resulting vector.

The technique above scales as $O(n \log(n))$ where here n is the length of a stationary period. In the case where $n \gg n_c$ we can do even better than this. As shown above, each time we do a circulant matrix multiply in place of a banded Toeplitz matrix multiply there is corrupted data within one bandwidth of either end of the resulting vector. We can use this fact to break the problem up into two sub-problems where two circulant matrix multiplies are performed, each of $n/2 + 2n_c$ length, and each producing correct results for $n/2$ elements. The vectors multiplied would be padded with zeros on the two ends of the original vector,

as before, but the end of the first vector would be extended with the beginning of the second half of the original, and the beginning of the second vector would be padded with the end of the first half of the original vector. This idea can be extended further and the problem can be broken up into as many sub-problems as we would like, to the limit where each circulant matrix multiply produces a single uncorrupted element for the output vector. The complexity of the suggested algorithm can be determined as follows: the cost of each FFT is $n_f \log(n_f)$, and the number of uncorrupted elements determined by an FFT is $n_f - 2n_c$. In order to calculate n_t uncorrupted elements there must be $\lceil n_t / (n_f - 2n_c) \rceil$ FFT’s performed, so the computational complexity is

$$O\left(\left\lceil \frac{n_t}{n_f - 2n_c} \right\rceil n_f \log_2(n_f)\right). \quad (22)$$

To a certain extent n_f is a free parameter and we can choose it to be optimal. This is done by minimizing the complexity. For simplicity of analysis we consider the function $h(n_f)$:

$$h(n_f) = \frac{n_f \ln(n_f)}{n_f - 2n_c} \quad (23)$$

$$h'(n_f) = \frac{1 + \ln(n_f)}{n_f - 2n_c} - \frac{n_f \ln(n_f)}{(n_f - 2n_c)^2} \quad (24)$$

$$h''(n_f) = \frac{2n_f \ln(n_f)}{(n_f - 2n_c)^3} - \frac{2(1 + \ln(n_f))}{(n_f - 2n_c)^2} + \frac{1}{n_f(n_f - 2n_c)} \quad (25)$$

Equation (22) and Equation (23) differ in that Equation (22) includes a discretization and a linear factor of $n_t / \ln(2)$, which determines the discretization. We will revisit the discrete nature of

the problem later, as there is another discretization to consider which impacts performance: the radix of the FFT. Note as well, that we only consider the cases where $n_f > 2n_c$, as all values determined by the FFT would be corrupted by the boundary conditions in cases where $n_f \leq 2n_c$. Setting $h'(n_f) = 0$ gives the following relationship between n_f and n_c :

$$n_f - 2n_c(1 + \ln(n_f)) = 0 \quad (26)$$

which, unfortunately, does not have an analytical solution for n_f in terms of n_c . We can solve for n_c , however, and check that $h''(n_f) > 0$ at this critical point, and this is shown in Appendix A.

In practice, radix two FFT’s are significantly faster than FFT’s of vectors of a length with a more elaborate factorization than simply a power of two. There is also no sense in choosing an FFT length that is more than twice the length of the longest stationary period to which it will be applied. As a result, we would like to choose the smallest power of two larger than the longest stationary period. If this value of n_f gives an $h'(n_f)$ which is positive, then decrease n_f by a factor of two until $h'(n_f/2) < 0$ or $n_f/2 < 2n_c$. This value of n_f is the length of the FFT used by MADmap in the case where the user has not specified a length by way of an environment variable⁵.

MADmap uses the FFTW library by default (Frigo & Johnson 2005), however at compile time it is also possible to specify the ACML library to do FFT’s. The ACML library is significantly faster than FFTW on AMD’s Opteron platform. Future extensions to MADmap will allow the use of the Intel Math Kernel library and IBM’s libmass which are other common high performance math libraries which include FFT functionality.

5.3. Compressing the pointing matrix

The pointing matrix is at the core of our time stream model as outlined in Equation (1). This matrix determines how a time stream of data observed by a detector relates to the discretized signal z . In its simplest form the pointing matrix can have one non-zero per row with value unity. The column assigned this unity value is determined by the pixel index of the element in the map that

is being observed by a detector at the time sample associated with the row. More sophisticated pointing matrices result when there is polarization sensitivity, or when the pointing matrix includes information about the detector beam sensitivity pattern. Each row of the pointing matrix determines the linear combination of the discrete signals being measured that were observed in a particular time sample.

As discussed in the introduction, the compression of the pointing matrix is critical to reducing the memory requirement, especially for analysis of data collected by contemporary CMB experiments with large numbers of detectors on a single focal plane. The calculation of the “right hand side” (RHS): $A^T N^{-1} \gamma$, uses γ , which is a length n_t vector, but this vector is used only once with a single pass through the time stream, so there is no need to store all of γ in memory simultaneously. The data can be read into small buffers, reduced to pixel domain data, and then overwritten with the next buffer of data.

The pointing matrix A , however, appears in the right hand side, and twice in the linear system inverted, which means that A is used on each iteration of our PCG solver. The simplest solution to this problem is the “high memory mode” of MADmap, where the sparse representation of A is stored concurrently in memory (in a distributed fashion) for the entire execution of the application. This method is fast, but can be overwhelmingly memory intensive, as the memory requirement scales as $O(n_t)$.

One method of averting this problem is to attempt to read the pointing matrix into memory from disk on each iteration of the PCG, but for almost every system configuration this will result in an I/O bound problem, and leave the processors idle while they wait on the disk subsystem. We have not yet attempted to use the asynchronous I/O options afforded by the MPI-2 standard, but a better solution exists which avoids repeated reading altogether while requiring a more modest memory footprint than is required for holding all of the detector pointing in memory simultaneously.

To overcome this problem, we make use of the fact that our pointing matrix is derived from data which is smaller than data required for the sparse representation. The compression of the pointing

⁵The FFT length environment variable: `MM_FFT_LENGTH`

matrix is experiment and signal specific, but in very broad terms, MADmap can work with any representation of compressed pointing that is sampled at a constant rate with a fixed number of double precision floating point numbers per sample. These data can be ingested by the GCP library which will produce detector-sampled pointing in row compressed sparse form (column index and weight pairs).

The pointing matrix for CMB experiments is often derived from telemetry data which measures the direction in which some fiducial center of the focal plane is pointed at a rate that is significantly lower than the detector sample rate. This is true for both real data sets and often for simulated data as well. The sparse representation of A is derived by an interpolation of the bore-sight pointing to a detector sample rate, and a rotation of the bore-sight pointing to each detector’s relative offset. This location is then discretized into a pixel index and assigned a weight, which usually differs from unity if the detector is polarization sensitive and the calculation of this weight is experiment specific.

In the past, when the number of detectors being analyzed simultaneously was more modest, the pointing solution for each detector would be stored on disk at the detector sample rate. This would sometimes be stored as ordinates (e.g., Euler angles) or as a list of pixel indices (with or without weights depending on the experiment’s capacity to measure a polarized signal). Reading these detector specific pointing sampled at the detector sample rate can be quite costly, but is still a possible option in MADmap.

5.4. Pixel indexing and distributed signal vectors

Regardless of how the sparse pointing matrix is obtained, once it is constructed in terms of the global pixel indexing scheme it must be re-indexed to match the distributed local pixel indexing scheme. Every pixelation of the sky has some intrinsic mapping between an index value and a position on the sky, and likewise, any discretized signal will have a mapping between index and the element of the discrete signal. There are actually three different indexing schemes used by MADmap: the global indexing scheme which is intrinsic to the discretization of the signal, the ob-

served indexing scheme which includes only those index elements which are observed in any processor’s data, and the local indexing scheme which includes only those index elements which were observed within the local processor’s data.

In order to distribute the signal vectors over the processors, each processor stores only those signal elements that are observed during the samples that are assigned to it, and all local signal vectors are indexed with the local scheme. MADmap stores two vectors that are used for mapping between indexing schemes. These are both the length of the number of locally observed pixels, and map from local index to observed index and from local index to global index. In order to use these vectors to map from global or observed index to local index, a binary search of the appropriate vector is done. This re-indexing is done every time the sparse pointing matrix is constructed from compressed pointing data. This requires a binary search of the locally observed pixel index for each time sample which has a computational complexity of $O(n_i n_t \log(n_z))$ operations. These are integer operations and do not contribute to the total flop count *per se*, but do consume clock cycles none the less.

In order to construct the index remapping vectors without ever allocating a full n_z length indexing vector, some bit operations are used. A bit array is allocated that has one bit for every global pixel index (n_z bits). The elements of this array are set to one or zero depending on if the index is observed within the local pointing matrix. This array can be used to construct the mapping from local index to global index. This array is then collectively reduced using `MPI_AllReduce()` with the `MPI_BOR` operator after which each processor has a bit vector that tells which pixels were observed within the data on all processors, and this bit array can be used to construct the mapping vector from local to observed pixels.

5.5. Communication patterns

Given the size of CMB data sets, MADmap is intended for parallel machines, from small clusters to the most massively parallel systems extant. Both time-ordered and pixel-domain data are distributed over the processors, and MADmap uses the standard Message Passing Interface (MPI) for inter-processor communication. Since the avail-

able memory will vary hugely depending on the number of processors being used to solve a particular problem (from tens to tens of thousands at the time of writing, with hundreds of thousands on the immediate horizon) and the available memory per processor (typically from 256MB to 4GB), MADmap provides a number of options to trade additional calculation for reduced memory.

Fundamentally, there are three communication operations in MADmap. The first comes up in the case where each processor has computed the contribution to a map vector from the time samples assigned to it in the computation of the operation of the pointing matrix. The sub-maps on each processor must be summed with the sub-maps on all other processors. Note that each processor contains a subset of the observed pixels that is overlapping with the subset of observed pixels on other processors. This computation, in the end, is computed with a series of `MPI_AllReduce()` calls. Each call is done on a fraction of the entire observed map, and each processor fills the reduction vector with the value it computed, or zero if the pixel was not observed in the processor’s time stream. After the reduction is completed, the results that are pertinent to the processor are stored, and the vector is overwritten with the next buffer to be reduced. This operation is called `MM_SomeReduce()`. This is, by far, the most costly communication operation. It scales like $O(n_z \log(n_{\text{proc}}))$ where n_z is the number of observed pixels, and n_{proc} is the number of processors. This must be done once on each iteration of the PCG algorithm.

The other two communication operations depend on the concept of “primary pixels.” In MPI, each processor available to an application is assigned a rank which is an integer in the set $\{0, 1, \dots, n_{\text{proc}} - 1\}$ so that every processor has a unique rank and there is a sequential ordering of the processors. A processor’s primary pixels are defined to be those pixels which are observed within the time stream distributed to the processor, and are not observed within the time stream distributed to any lower rank processor. This determination defines a disjoint division of the pixels over the processors that is comprised of a subset of the fundamental distribution of the pixels over the processors. To determine the primary pixels, an `MM_SomeReduce()` is called on a vector

that is set to be the processor’s rank if the pixel is observed by the processor or the total number of processors in the case where the pixel is not observed within the processor’s time stream, and the reduction operator is `MPI_MIN`. After the call to `MM_SomeReduce()`, the reduced vector can be used to determine as primary pixels all of the pixels that are set to the value of the processor’s rank.

The second operation is very similar to the first, except that it is used only in the writing of maps to disk. When writing a distributed map vector to disk there are a series of calls to `MPI_Reduce()`. This sequence of reductions effectively constitute single reduction operation on a map of all observed pixels while limiting the size of the vector used in the `MPI_Reduce()` call and thereby mitigating the memory requirement. In this operation each processor sets the map value to its stored value if the pixel is a primary pixel, and sets it to zero if the pixel is not a primary pixel of the processor. In this way the root processor collects the map and writes the buffer to disk between each call to `MPI_Reduce()`.

The final operation is the computation of the dot product of two distributed map vectors. This is done by computing the local contribution to the dot product by primary pixels on the processor, and then an `MPI_AllReduce()` is called on the one double precision floating point element to evaluate the complete dot product combining calculations from each processor. Because this requires a single call to `MPI_AllReduce()` on a single element for each dot product, this communication cost does not account for a significant amount of the run time.

5.6. Memory Use and Computational Complexity

MADmap’s computational work can be segmented into several distinct operations. The dimensions of the problem to be solved determine the relative cost of the operations, but we will discuss the operations that typically are the most time consuming. Those operations which are done on each iteration of the PCG tend to dominate the run time because the factor of the number of iterations is usually between one and two orders of magnitude. The dominant term in the overall computational complexity of MADmap in all modes of operation is $O(n_i n_t \log(n_c))$, which is de-

terminated by the computation of the FFT's, and this computation constitutes a significant portion of the run time. A portion of the run time is spent constructing and acting with the pointing matrix and, in low memory mode, these operations have an operational complexity of $O(n_i n_t n_{nz}(1 + \log(n_z)))$ with a significant pre-factor. This computation includes the expansion of the compressed pointing into the sparse pointing matrix, the re-indexing of the pixels to distributed indexing, and multiplying by the sparse re-indexed pointing matrix.

The complexity measures given below are distributed over the processors and MADmap has been scaled to run on tens of thousands of cores. MADmap is load balanced computationally and the memory distribution is balanced in all dimensions except n_z which is, nonetheless, distributed. MADmap has three different modes of operation which reduce the memory requirement at the expense of more computations. The operational complexity of the high memory mode is

$$c_h = O(n_i n_t \log(n_c)), \quad (27)$$

and the memory requirement is

$$m_h = O(n_z + n_t + n_{\text{proc}} m_n). \quad (28)$$

The operational complexity of the low memory mode is

$$c_l = O(n_i n_t (\log(n_c) + n_{nz} \log(n_z))) \quad (29)$$

and the memory requirement is

$$m_l = O(n_z + r_p \Delta t + n_{\text{proc}} m_n). \quad (30)$$

The operational complexity of the extremely low memory mode is

$$c_e = O(n_i (n_t (\log(n_c) + n_{nz} \log(n_z)) + n_b n_c \log(n_c))) \quad (31)$$

and a memory requirement of

$$m_e = O(n_z + r_p \Delta t). \quad (32)$$

The variable m_n is the per processor memory requirement for the noise filters and depends on the data distribution as given by the variables m_{ns} and m_{nc} defined in Section 5.7. Note that low memory mode footprint is nearly invariant with the number of detectors and the footprint of the extremely

low memory mode is completely invariant with the number of detectors. Next generation CMB experiments will operate with large numbers of detectors sampled at a high rate so the memory savings afforded by low memory mode will be critical to the tractability of the maximum-likelihood data analysis of these next generation experiments.

5.7. Disk Usage

The disk is accessed for five purposes, three of them reading: detector time streams, pointing information, and noise filters; and two of them writing: checkpointing, and the final maps. There are many options which allow most of this disk access to be minimized. In some cases the time stream data are simulated at run time using the M3 on-the-fly simulation capabilities, and require only a small amount of input data from disk (usually in the form of maps). The pointing information can take on a wide variety of forms. Noise filters can be input parametrically, and in this case the filters are calculated at run time without reading from disk. Checkpointing is optional, and the frequency can be chosen, but by default occurs after every 20 iterations. The output of the final maps is a relatively small amount of data, and only one processor writes the final maps to disk.

The detector time stream samples are distributed in a balanced way over the processors independent of the data distribution mode chosen. Each processor reads or simulates a fraction of the total volume of the detector time samples divided by the number of processors. Recall that there are three data distribution modes in MADmap: concatenated, stacked and multi-stacked. The choice of distribution has an impact on the amount of telescope pointing data read, and the number of noise filters read and stored, but does not impact the volume of detector data required by each processor. If the time stream data are read from disk, then every processor reads

$$d_t = O\left(\frac{n_t}{n_{\text{proc}}}\right) \quad (33)$$

samples which are typically stored in eight byte precision.

The amount of pointing data to be read from disk depends on how the MADmap job was configured. In the minimal case, MADmap is run in the

stacked data time stream distribution, and telescope centroid pointing sampled at a slow rate is used and interpolated to detector pointing at run time. The amount of reading required in this case is the number of telescope centroid pointing samples divided by the number of processors. The use of the concatenated data distribution requires an additional factor of the number of focal plane detectors of extra reading for centroid pointing since different processors are analyzing data from the same time period. The telescope centroid pointing data in the concatenated data distribution are not balanced and different processors will require the same pointing data. When using telescope centroid pointing it is usually optimal to use the stacked data distribution. In the typical case of reading telescope centroid pointing and using the stacked distribution MADmap reads

$$d_{ps} = O\left(\frac{n_t r_p}{n_d r_d n_{proc}}\right) \quad (34)$$

elements of the telescope pointing. Each element of telescope pointing is typically between three and six numbers stored in eight byte precision. Using the concatenated distribution requires another factor of n_d on each processor bringing the number of elements to

$$d_{pc} = O\left(\frac{n_t r_p}{r_d n_{proc}}\right). \quad (35)$$

If individual detector pointing is read the number of elements required is

$$d_{pd} = O\left(\frac{n_t}{n_{proc}}\right). \quad (36)$$

The potential hazard of the stacked data distribution lies in the reading and memory requirement associated with the noise filters. In the concatenated distribution each processor has to load and store only order one noise filter requiring

$$d_{nc} = m_{nc} = O(n_c) \quad (37)$$

elements read from disk stored in eight byte precision by each processor. In the stacked distribution each processor loads and stores a noise filter for every detector requiring

$$d_{ns} = m_{nc} = O(n_d n_c) \quad (38)$$

elements stored and read from disk. To compromise between these noise filter requirements and the telescope centroid pointing requirement the multi-stacked distribution is advised. An exceptional case for the filter memory requirement occurs if the same noise filter is used for every stationary interval analyzed, and in this case MADmap stores just one filter, regardless of the data distribution. This exception is most useful for simulated data.

6. Using MADmap

The MADmap algorithm, its implementation, as well as the structure of the associated data abstraction (M3) and compressed pointing (GCP) libraries have all been designed to ensure maximal flexibility and broad applicability of the software to CMB data analysis and more generally to estimation problems. The range of problems that the MADmap software can be directly applied to is indeed very wide, and significant effort has been undertaken to ensure that the generality in the problem formulation and algorithm choices do not negatively impact the computational efficiency of the software. We will illustrate the efficiency issue in the next section studying two specific applications and compare it with some other similar codes in Section 8. In this section we describe a set of example problems to which MADmap can be directly applied. We include here only the kinds of runs which have actually been performed and their results validated on either simulated or real data.

MADmap's most notable flexibility is its ability to ingest and process an arbitrary pointing matrix. This is true at least on the algorithmic level, however the run-time and memory requirements will depend on the sparsity and structure of the pointing matrix, and these requirements will clearly set some constraints on the practical level. Nonetheless, MADmap permits performing runs which not only produce the sky signal maps, but also extract the unwanted parasitic contributions typical of many experimental data, as long as they can be expressed within the linear response model of Equation 1. The examples given previously demonstrate that those include cases of real practical interest.

(1) *Non-parametric synchronous signals.* In many applications there exists a parasitic signal of an in-

strumental or environmental origin which can be thought of as a unique function of some parameter. We will refer to those as signals synchronous with the respective parameter. Examples of such signals include the previously mentioned primary-mirror-chop-synchronous parasitic signal observed in the MAXIMA data, as well as ground or atmospheric pick up usually seen in ground-based experiments, (e.g., Kuo et al. 2004). If we denote such a parameter or set of those by ψ we can update Equation 1 to read,

$$\gamma = \nu + \zeta + \psi = \nu + Az + By \quad (39)$$

where B is a ‘pointing’ matrix of the parasitic signal, and y is a discretization of its amplitude. In the specific example of the primary-chop-synchronous parasitic signal, y may correspond to an orientation angle of the primary with respect to the gondola frame and $B_{t,p}$ is non-zero and equal to unity for all the time samples, t , for which the primary orientation fell in between an interval, $[y_p, y_p + \Delta y_p]$, defining the non-overlapping discretization (one dimensional ‘pixelation’) of the possible angles, y .

On replacing,

$$z \rightarrow \begin{bmatrix} z \\ y \end{bmatrix}, \quad A \rightarrow \begin{bmatrix} A & B \end{bmatrix}, \quad (40)$$

in Equation 1 we see that both Equation 1 and Equation 39 are clearly of the same form and therefore can be solved using the same algorithm as implemented in MADmap, provided that suitable input data properly describing the full pointing matrix of the problem are available.

(2) Parametric synchronous signals.

In some applications parasitic signal may not be synchronous with any easily identifiable external parameter but there may exist a linear parametric model which can describe the time-dependence of the signal, i.e., $\psi_t \equiv \psi(t; \{b_i\})$ and $\psi = Cb$. We note that the last equality may be in fact only an approximation, e.g., a result of linearization procedure around the anticipated values of the parasitic signal parameters, even if the latter are inherently non-linear. In those cases, the validity of the approach may need to be evaluated *a posteriori*.

On adding such a term to Equation 1, we again arrive at an expression similar to Equation 39, which in turn is equivalent to Equation 1 with

appropriately redefined pointing matrix and estimate vector, Equation 40.

We note that such an option is of great current interest. This is because the parasitic signal due to the rotating polarizers, such as e.g., half-wave plate. The signal of this sort is expected to be one of the major systematics the polarized experiments using this kind of technology, and accurately removing this systematic is crucial to achieving sensitivity levels required for a successful B-mode polarization detection. It has been shown (Johnson et al. 2007) that in cases of practical interest such a signal can be modeled with a couple of dozens of parameters and that a linear model can be indeed sufficient for such a purpose. Specifically, the particular model can be written down as,

$$\begin{aligned} \psi_{\text{HWP}}(t) &= \sum_{k=1}^8 (b_k + t b_{k+8}) \cos k\omega_t \\ &+ (b_{k+16} + t b_{k+24}) \sin k\omega_t, \end{aligned} \quad (41)$$

where ω_t denotes a known position angle of the polarizer. Thus for any time t , we recover,

$$C_{t,i} = \begin{cases} \cos i\omega_t & i = 1, \dots, 8; \\ t \cos(i-8)\omega_t & i = 9, \dots, 16; \\ \sin(i-16)\omega_t & i = 17, \dots, 24; \\ t \sin(i-24)\omega_t & i = 25, \dots, 32; \end{cases} \quad (42)$$

where C complements the sky signal pointing matrix as in Equation 40. The map-making solver will then estimate simultaneously both the sky signal (z) and the HWP parasitic parameters (b).

We note that, in the case of the rotating polarimeter, the parasitic signal is indeed synchronous with the polarizer orientation and could also be subtracted using the approach described in case (1) above. Applying the parametric model as described here, however, allows us to reduce the number of extra degrees of freedom introduced to the problem and therefore to achieve higher precision of the recovered final maps of the sky. It also permits for the avoidance of discretization effects, and these are particularly important for cases involving rapidly varying systematics. We also point out that the block of the pointing matrix, as defined in Equation 42, is dense, and therefore poses a particular challenge to the standard way of implementing the pointing and unpointing operators discussed earlier.

(3) *'Destriping' runs.* In some particular applications the time-domain noise can be effectively modeled as white noise plus a series of random offsets assigned to some predefined time intervals. This was first discussed in the context of Planck-like experiments (Janssen et al. 1996) and gave rise to so-called destriping algorithms (Delabrouille 1998; Maino et al. 1999; Keihänen et al. 2004). It has been shown that in the Planck case the destriper achieves a competitive precision at a fraction of the numerical load (Poutanen et al. 2006; Ashdown et al. 2007a; Stompor & White 2004). The approximate time-order data model in this case reads

$$\gamma_t = \nu + \zeta + \omega = \nu + Az + Bo \quad (43)$$

where ν is uncorrelated, piecewise-stationary noise, ω_t is an offset added to a sample t , and o_p is an offset common to all samples in a time interval p . B is an offset pointing matrix, essentially defining the time intervals associated with each of the offsets denoted as o_p . Using both the pointing matrix and the solution (map) vector extended as in Equation 40 MADmap can therefore simultaneously estimate the sky signal and the offset amplitudes, assuming that the used time intervals conditions do not lead to a singular system of equations. We can further assume that the noise is not merely stationary, but *white*, and thus that N is diagonal, which is a basic assumption in the standard destrippers (Keihänen et al. 2004). In spite of its more complex pointing matrix, this kind of run will benefit considerably from the fact that no FFT is needed for performing any of the noise kernel convolutions, and this results in a significantly shorter run-time when compared to the run incorporating the more complex time-stream model. As mentioned before, at least in some specific cases, the speed-up may indeed be achieved at no substantial loss of precision in the final sky maps. We note however that though such MADmap run would indeed be significantly faster, than a full MADmap run with a complete noise model, it would not reach the speed typical of custom-made destrippers. Nevertheless, the attractive feature is that MADmap provides in a single package both functionalities as well as entire spectrum of intermediate options.

(4) *Multi-resolution map-making* As MADmap does not interpret or make any assumptions about

the pixel signal and/or pixelation schemes, it straightforwardly permits for mixing sky pixels of different resolutions, for instance, enabling a higher resolution for sky areas with particularly high signal-to-noise ratio. It also accepts different resolutions for different Stokes parameters. The latter fact is again particularly interesting in the light of forthcoming polarization experiments based on total power detectors. In such cases the measured signal is a linear combination of all three Stokes parameters. Map-making therefore attempts to unscramble it to estimate all three of them simultaneously. For the CMB, the power contained in the total intensity mode, I , is significantly higher than that in the polarization. That has two consequences. First, the total intensity map could be pixelized with high resolution pixels retaining the same signal-to-noise on the pixel scale as for the polarization. Moreover, given that sky signal is assumed to be constant on the pixel scale, any departure from such assumptions (e.g., due to residual sub-pixel power) may result in signal leakages between different Stokes parameters. The intensity signal is much higher than the polarization signal, and therefore any sub-pixel power which is a small fraction of the intensity may be substantial when compared with the polarization signal. By over-pixelizing the intensity we can lower sub-pixel power and mediate the leakage of this power to the Q and U basis. In this way we reduce the aliased sub-pixel intensity signal present in the estimated Q and U maps.

Such an effect has been indeed observed in simulated cases (Ashdown et al. 2007a). MADmap's ability to accommodate different pixel resolutions for different Stokes parameters allows us to robustly bypass such problems by reducing the size of the I pixels and with it the amount of the power leaked from I to Q and U .

We note that all these capabilities are unique compared to other CMB map-making software packages.

7. MADmap Map-Making Examples

We will describe the tests that have been performed on MADmap and highlight the functionality provided by the M3 data abstraction layer, and the Generalized Compressed Pointing (GCP) library. MADmap has been run on an array of

real and simulated data. In this paper, we would like to describe two large runs that demonstrate MADmap’s capabilities and capacity. Both of these runs are analyses of simulated data, the first a year-long Planck satellite mission (The Planck Collaboration 2005), and the second a two-week EBEX balloon-borne measurement (Oxley et al. 2004; Grainger et al. 2008). In the following we start from a short description of features of each of the experiments and their data set and continue with a detailed discussion of MADmap map-making run performance.

7.1. Planck

Planck is a ESA/NASA satellite, which will carry on board two instruments: Low and High Frequency (LFI and HFI, respectively) and a total of 74 independent detectors (54 of which are polarization-sensitive) measuring the sky signal in 9 frequency bands. Over a period of fourteen months Planck will observe the full sky twice⁶ at a resolution dependent on the frequency band, ranging from 33’ at 30GHz down to 5’ at 217GHz and above. The detector sampling frequency likewise ranges from 32.5Hz at 30GHz up to 172Hz at 100GHz and above. Consequently, the Planck time ordered data set will consist of roughly 325 Giga-samples, from which 23 maps will be derived (where a map is counted for each stokes parameter and each observing frequency). The number of sky pixels per map will be as high as 50 Mega-pixels for the high frequency, high resolution channels. With only two full sky coverings, and modest sampling rates, Planck will achieve a relatively low density of observations per unit sky area. This results in a relatively low signal-to-noise ratio at the resolution scale of the recovered maps, particularly when considering the faint magnitude of the polarization signal.

The Planck simulations used here were calculated with the Planck Level S simulation pipeline (Reinecke et al. 2006). By default this software generates and writes to disk telescope pointing files and detector data time streams. For some of the tests, we used the Level S package to simulate and store only the telescope pointing information, while the time domain data themselves

⁶A decision on extending the mission to support two further coverings of the sky is pending.

were generated only at run-time using the M3 on-the-fly simulation capability. The full Planck focal plane analysis was the largest scale MADmap run to date, which turned 325 Giga-samples into estimates of 150 Mega-pixel amplitudes.

7.2. EBEX

EBEX is a balloon-borne experiment which will collect data during a roughly two-week long circumpolar flight in Antarctica. It will carry on board 1406 detectors observing in 3 different frequency bands: 140, 220 and 410GHz. The resolution at each frequency will be 8’. The sampling frequency is set to 190Hz. During its flight, EBEX will target a small area amounting to roughly 1% of the entire sky. Due to its much larger number of detectors and higher sampling rate, the total length of the EBEX time ordered data set is comparable to the Planck baseline mission. The adopted observation strategy will result in a very deep integration of the probed sky area reaching up to millions of measurements per beam-size pixel. Consequently, the recovered maps will have high signal to noise ratio at the resolution scale. This is driven by the scientific goals of EBEX, which are to detect and characterize the minuscule CMB B-mode polarization signature. The size of the maps produced from the EBEX data will be limited to 10^5 pixels, i.e. half a percent of one of the Planck maps. For the EBEX simulations we use the M3 simulation capability to generate time stream data on the fly when MADmap makes data requests.

7.3. Performance analysis

The simulations presented here were conducted at the Department of Energy NERSC supercomputing center on the Cray XT4 named Franklin. Franklin has 9660 compute nodes, and at the time when the Planck full focal plane simulation was run in September 2007 these nodes contained one 2.6 GHz clock speed dual core AMD Opteron processor with 2 gigabytes of memory per core. When the scaling tests for the Planck and EBEX simulations were run in October 2008 the Franklin processors had been updated to quad core AMD Opteron processors running at 2.3 GHz with two gigabytes of memory per core. Franklin has a fast SeaStar2 switch interconnect, and runs the Lustre

file system to control 350 terabytes of usable disk space.

We performed a sequence of scaling tests on MADmap to show its performance on large data sets and computing at scale. These runs are broken into three cases. The first two are nearly identical simulations of the Planck telescope’s 217 GHz channel. For one of these simulations the data are precomputed and read from disk, and in the other case the simulation of the time stream is done at run time. The third case is a simulation of the EBEX experiment with data simulated at run time. Through these three simulations we show the performance on high resolution full sky data in the Planck case, and a small patch medium resolution very low pixel noise simulation in the EBEX case. By simulating data at the time of request we are demonstrating MADmap’s capacity for Monte Carlo simulation analysis with negligible disk use. We also present an analysis of a year of data collected by the entire Planck focal plane as a demonstration of computational capacity in both the pixel and time domains.

In the scaling runs each of the three cases was analyzed at four different processor concurrencies. For the Planck analysis these concurrencies were 2,196, 4,392, 8,784 and 17,568 processor cores, and the EBEX analyses were run on 1,920, 3,840, 7,680, and 15,360 processor cores. In the Planck scaling runs the number of time samples, n_t , was 7.6×10^{10} and the number of observed pixels in all three polarization maps, n_z , was 1.5×10^8 . In the EBEX case n_t was 1.6×10^{11} and n_z was 1.0×10^5 .

The results of these runs are shown in Figure 4. There are some particular features that stand out in the plots. These are strong scaling plots, therefore measured in processor seconds, and ideally these would be flat, implying total cost invariance with processor concurrencies. The cost of the computation is close to this ideal, which implies that the problem is well balanced. The input/output subsystem is very limited under the strain of large concurrencies of file requests and does not scale well. This is a known problem with contemporary supercomputers run at scale, and highlights the power of being able to simulate data at the time of request in order to avoid the I/O bottle neck. This point is clear when the time spent in I/O in the Planck disk case is compared to that of the Planck on-the-fly simulation case.

Communication cost for all sky high resolution maps is significant, but in the low pixel count case of EBEX the communication is sub-dominant. The communication cost is essentially linear with the number of observed pixels. The EBEX case has just over 100 thousand pixels observed, and the Planck case has 150 million pixels observed. Over the concurrencies probed, the range of pixels spans the space where communication is significantly smaller and larger than the computation cost. The Planck case scaled up to over 10k processors shows the limitations of the parallelism used for the pixel domain data. Work is ongoing to improve this limitation so that MADmap will scale to hundreds of thousands of processors and hundreds of millions of pixels.

The computation of the pixel look-up actually requires fewer calculations at higher concurrencies because the complexity is a function of the number of locally observed pixels which decreases as the time stream is divided more finely. We can also see the effects of memory locality and cache misses in the computation of the pointing. This is highlighted by comparing the Planck runs done with the Healpix nested scheme and the Healpix ring scheme (Górski et al. 2005). In the nested scheme, pixels nearby on the sky have similar pixel indexes, and therefore show better cache performance in the calculation of the action of the pointing matrix.

In the case of the Planck full focal plane run described earlier, which constituted the largest MADmap run performed to date, the analysis was done in the concatenated data distribution in low memory mode on 16,384 cores and completed in 32 minutes. In this run, the expansion of the compressed pointing by the GCP library consumed 19.0% of the run time. The calculation of FFT’s with the ACML library consumed 11.9% of the wall clock time. Pixel re-indexing constituted 6.3% of run time and multiplying by the sparse pointing matrix 4.9%. Outside of these calculations, 24.0% of run time was spent on communication of signal vectors, 23.1% on reading simulated time streams from disk, and 3.8% on writing maps to disk.

A sample of the results of the MADmap runs analyzing the simulated EBEX and Planck data sets is presented in Figures 5 & 6, respectively.

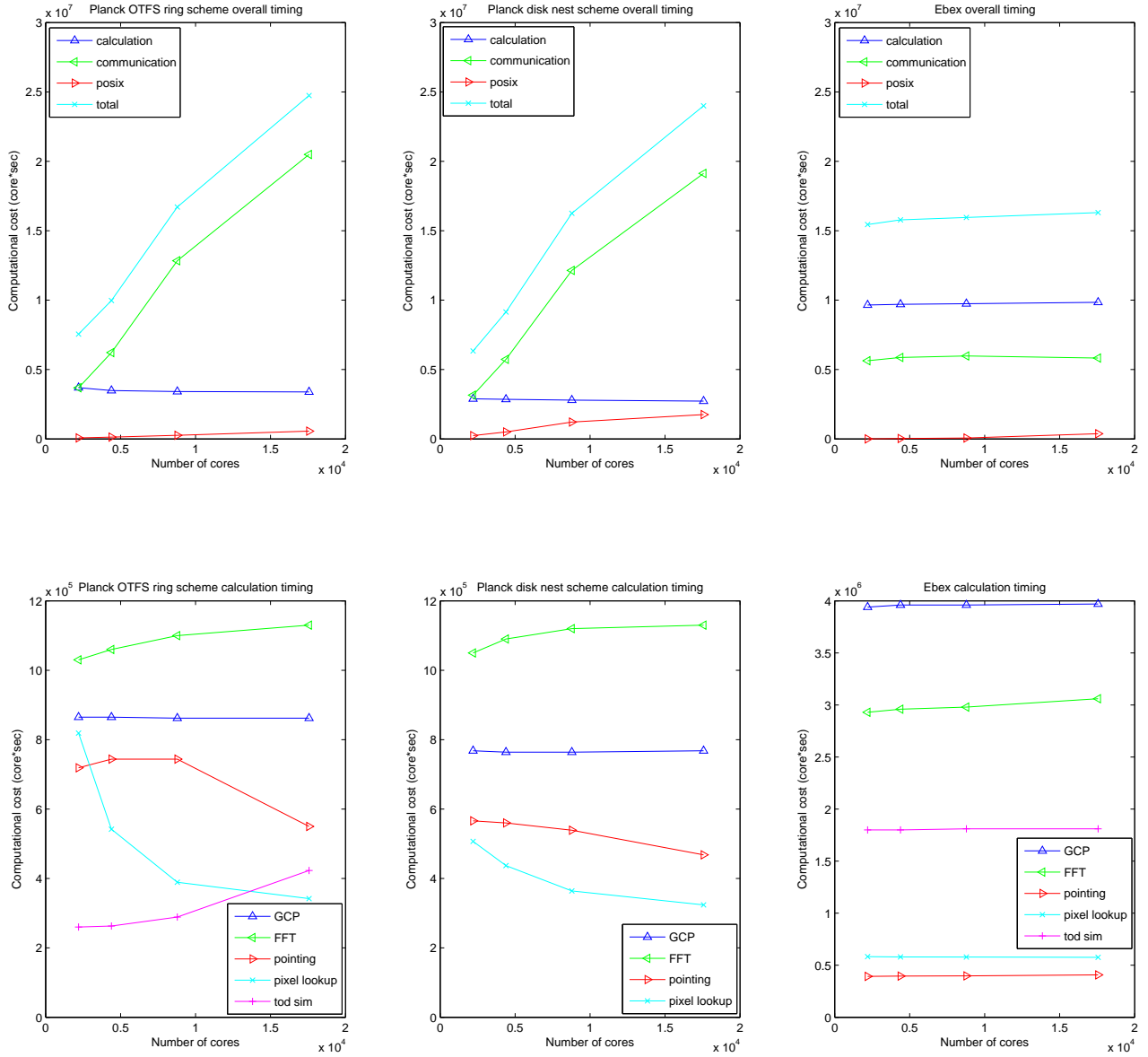


Fig. 4.— This figure plots the results of the three scaling tests that were performed. Each run is represented by two plots. One measures the overall cost of calculation, communication and I/O; the other breaks down the time spent doing computations between the algorithms that comprise the computations.

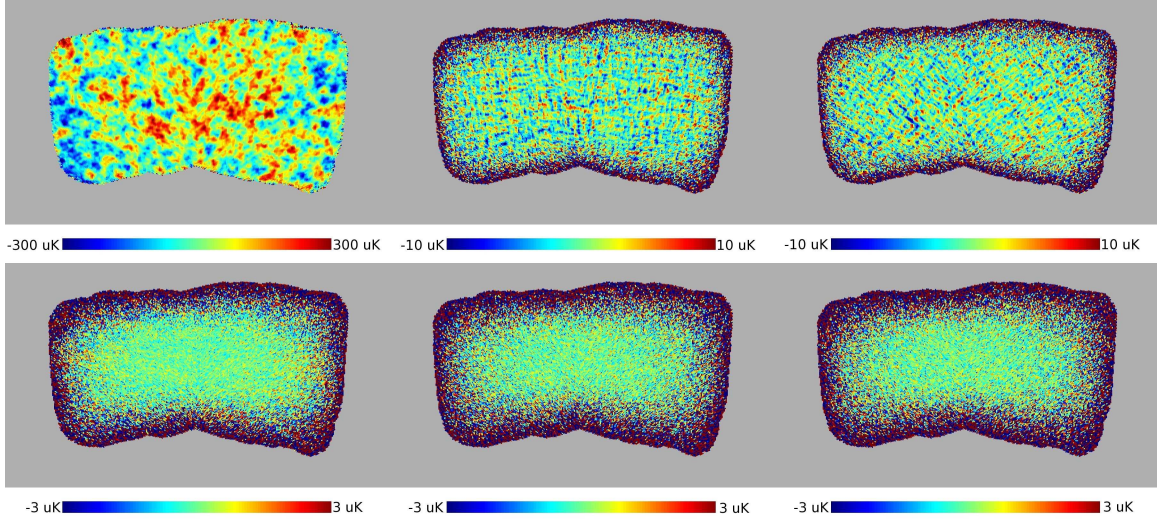


Fig. 5.— This figure shows the map resulting from the EBEX scaling runs, which recovered the polarized sky signal from 1.6×10^{11} time samples. The color scale is given in units of μK thermodynamic temperature. Plotted in the top three panels are the I, Q and U polarization components, and below each map is an image of the difference with the input signal map used to generate the simulation.

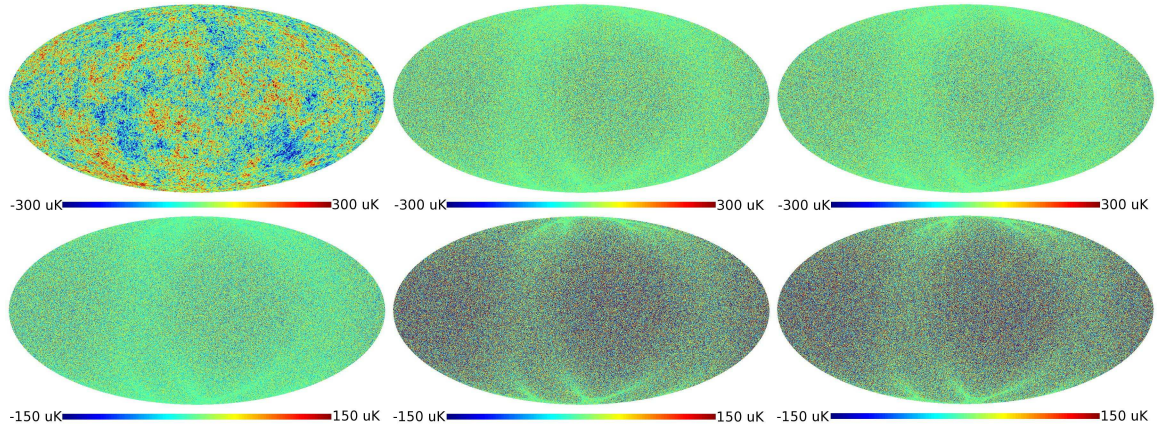


Fig. 6.— This figure shows the map resulting from the Planck scaling runs. The color scale is given in units of μK thermodynamic temperature. Plotted in the top three panels are the I, Q and U polarization components, and below each map is an image of the difference with the input signal map used to generate the simulation. Note that for the Planck 217 GHz channel the Q and U maps are noise dominated when produced at high resolution (Healpix nside parameter of 2048). The data set simulated for this run comprised of 7.5×10^{11} samples divided between 74 detectors and 9 frequency bands.

8. Comparison With Other Codes

Map-making is one of the principal constituents of the data analysis pipeline of any CMB experiment. Consequently, there has been a significant body of work devoted to different algorithmic and implementation aspects of the map-making problem, (e.g., Wright et al. 1996; Janssen et al. 1996; Tegmark 1997; Delabrouille 1998; Borrill 1999; Oh et al. 1999; Maino et al. 1999; Doré et al. 2001; Stompor et al. 2002; Hinshaw et al. 2003; Keihänen et al. 2004; Stompor & White 2004; Armitage & Wandelt 2004; de Gasperis et al. 2005; Keihänen et al. 2005; Poutanen et al. 2006; Patanchon et al. 2008; Armitage-Caplan & Wandelt 2008; Sutton et al. 2009; Kurki-Suonio et al. 2009), and many numerical map-making codes have been developed over the years and reported in the literature. Few of those have ever been implemented for a massively parallel architecture. Still fewer of those have been applied to the data sets of the size and complexity as expected from Planck and the next generation of the CMB experiments. Only some of those codes are flexible and general enough to be applicable to a realistic CMB data set as produced by scanning experiments. To the best of our knowledge none allows for fully arbitrary pointing matrices as MADmap does, instead usually relying on its hard coded, parametrized version appropriate for some specific instrument. Moreover, although some of the existing codes are used by larger groups of researchers, none is readily available in the public domain.

Over the past few years the Planck CTP working group has undertaken a coordinated effort to compare some of the existing map-making codes. The final stage the comparison involved 5 codes, including 2 Planck-specific codes referred to as 'destripers' and 3 maximum-likelihood codes including MADmap. The aim of these comparisons was to first demonstrate the software's capacity to deal with the requisite volume of data, and then the precision of the results, and the resource requirements were measured and compared.

The results have been published in series of papers (Ashdown et al. 2007a,b, 2009). Those results validated MADmap, which has been shown to produce maps virtually indistinguishable from those of the other maximum-likelihood map-makers and the produced maps were consistent with input

maps used to generate the time ordered data simulations. The MADmap results were also found to be very similar to those of the destripers, though MADmap was somewhat closer to the input map. This small advantage of the maximum-likelihood codes is understandable and expected as they are designed to produce minimum variance, optimal maps. In terms of the resources, the superior CPU and memory performance of MADmap with respect to other maximum-likelihood estimators has been duly demonstrated in Ashdown et al. (2009). The destripers, devised as Planck-specific map-makers (but see Sutton et al. 2009), gain on speed and/or memory requirements at the price of their generality, and therefore were capable of delivering a comparable performance to MADmap at the fraction of its resource requirements. We note that the resource comparison presented in Ashdown et al. (2009) was obtained using a data set of a rather modest size with a total number of samples $n_t \sim 10^9$ and pixels $n_z \sim 9 \times 10^6$ including maps of the three polarization Stokes parameters.

In the particular simulation presented in (Ashdown et al. 2007b), when run in large memory mode, MADmap was found to require less than half of the CPU resources of the other two maximum likelihood map-makers in the comparison (44% of the CPU resources required by MapCumba, and 40% of the CPU resources required by ROMA), while MADmap had a slightly higher memory footprint. MADmap's slightly higher memory usage is because MADmap stored a different noise filter for each stationary period where the other codes assumed a single noise filter for the entire data set. When run in low memory mode MADmap's memory footprint was nearly one quarter the size of the other two maximum likelihood implementations, and the CPU resources required were about two thirds of those required by the other maximum-likelihood solvers (68% of the CPU resources required by MapCumba, and 61% of the CPU resources required by ROMA). This paper complements the results published in the CTP papers by showing the scalability of the MADmap code to the large concurrences and its performance while facing the most voluminous forthcoming data sets as well as highlighting its additional features not tested in the CTP runs.

The majority of the codes and methods dis-

cussed above work efficiently, or typically only, in pixel domain. Harmonic space map-makers have been also recently considered (Armitage & Wandelt 2004; Armitage-Caplan & Wandelt 2008) though demonstrated so far only in the cases with uncorrelated time-domain noise. The potential advantage of the harmonic approach is that it allows to correct for a potential beam asymmetry in a more straightforward manner. We note that such a beam correction can be at least to some extent resolved also in the pixel domain (Burigana & Sáez 2003) though would require an appropriately defined pointing matrix. Given that, MADmap can be a tool of choice for performing such a study in the future.

9. Conclusions & Future Work

This paper offers an in-depth description of the MADmap software application, describing the details of the algorithm and the massively parallel implementation. What is presented in this paper is MADmap’s capacity to scale to very large problems and very large processor concurrencies. We discussed the variety of modes in which MADmap can be run, which allows for trade-offs between CPU and memory consumption. One of the main features that sets MADmap apart from other map-makers is the wide flexibility in the data model that enables support for any sparse linear model of the signal to be estimated. This highly adaptable model for the signal is further enabled by the GCP library which provides a modular plug in architecture that can be used to compute the sparse linear model from compressed data. The functionality provided by GCP is what enables MADmap’s low memory mode.

Recall that, in low memory mode, the sparse pointing matrix is created in a buffered way from cached compressed data through the GCP library. When MADmap is run in the stacked data distribution, the compressed data can be reused for multiple detectors, and in this way reduces memory and sometimes CPU requirements for GCP. GCP’s modularity allows for the addition of features which can be used to accomplish a wealth of science goals. One interesting use is the calibration with a known signal (like the CMB dipole) as a byproduct of map-making while consistently accounting for the extra degree of free-

dom added by this estimation. Another possibility is to do component separation during map-making to produce maps of different astrophysical processes from time streams of data collected at different observing frequency bands. This can be accomplished if the linear scaling terms for the projection from frequency band to astrophysical component are known *a priori*, and a GCP module is added to produce a sparse pointing matrix that corresponds to this projection. A capability which currently exists is the removal of systematic effects corresponding to a linear scaling of a measured template. These systematic effects range from the temperature of the cold stage of the cryogenic electronics, to a measured template for thermal pick-up from the ground as a function of a ground-based telescope’s orientation, or any other *a priori* known signal to be marginalized from the output maps. GCP also promises the ability to deconvolve compact beam effects during map-making by representing some portion of the beam profile in the pixel domain in the sparse pointing matrix. This can be used to account for asymmetries in the beam, through the combining of detectors with disparate beam profiles into a single map (usually required for component separation during map-making), or can even be used to deconvolve in the pixel domain the effects of a bolometric detector’s response curve in the time domain.

MADmap is capable of solving massive problems quickly and efficiently given appropriate computational resources and such large runs have been presented in this paper. MADmap is a useful and efficient tool that can be run on much more modest computing resources, and the scale of the runs presented should not misinform the reader about minimum resource requirements of MADmap. MADmap can be quite computationally efficient on small cluster sized resources, and when run in low memory mode it can reduce large time ordered data sets in core memory. The limiting factor in this case is run time, but at low concurrencies, and when using a reasonable communication fabric, MADmap is very efficient. In addition, often on these small clusters a limited user pool allows for the execution of jobs with very long wall clock times, and in these situations MADmap can tackle non-trivial problems with a modest computer. MADmap implements efficient

check-pointing, and this allows for the exploitation of long-running jobs without fear of wasting resources in the case of a system failure during execution.

The massively parallel computing community is on a road map to push its systems to the exascale, which is 10^{18} calculations per second, by about 2018. The primary impediment to scaling up MADmap to the exascale and beyond is the collective communication calls used to reduce maps. It is the subject of ongoing research as to optimize our collective communication to take best advantage of character of our data distribution, its sparsity and the communication fabric topology.

MADmap does not currently have a facility for modeling correlations in the noise that may exist between different data sets, which are to be processed simultaneously, such as measurements coming from different detectors of the same experiment. Such correlations may be due to electronic cross talk, thermal drifts of a cryogenic focal plane, or in the case of ground based experiments, atmospheric noise that is seen by the focal plane simultaneously. This correlations can be very important to some collected data sets, and incorporating this functionality is a focus of ongoing work.

In future publications we will present more applications of MADmap in particular those demonstrating the GCP library functionality on real and simulated data. A package containing MADmap and all its dependencies is available for download at the LBNL CodeForge website⁷. MADmap, GCP and M3 are free software and distributed under the GNU public licence agreement with hope that it will become a software package of the choice for the CMB community for an efficient computation of the microwave sky maps.

We are grateful to NASA (through the Planck Project) and DoE for funding and facilities. This research used resources of the National Energy Research Scientific Computing Center, which is supported by the Office of Science of the U.S. Department of Energy under Contract No. DE-AC02-05CH11231. Thanks to Charles Lawrence for his help and guidance in this project and the submission of this paper. We acknowledge the use

of simulations of telescope pointing provided by the Planck and EBEX collaborations. In particular the simulation of the Planck mission was done by the simmission (Reinecke et al. 2006) application primarily written by Daniel Mortlock and managed by Martin Reinecke. The sky scanned in the Planck simulation was provided by the Planck collaboration and is the model derived by the Planck foregrounds working group. The EBEX telescope pointing simulation was provided by Samuel Leach, and the sky simulation was provided by Nicolas Ponthieu. The parametrization of the noise properties of EBEX was provided by Shaul Hanany, and the simulation was generally a product of the EBEX data analysis working group.

⁷LBNL CodeForge:
<https://codeforge.lbl.gov/projects/cmb/files>

A. Proof that critical FFT length minimizes complexity of convolution algorithm

Proof. In Section (5.2) we need to show that $h''(n_f) > 0$ for our critical value of n_f so as to insure that our critical point minimizes the complexity. Recall that $h''(n_f)$ is defined as

$$h''(n_f) = \frac{2n_f \ln(n_f)}{(n_f - 2n_c)^3} - \frac{2(1 + \ln(n_f))}{(n_f - 2n_c)^2} + \frac{1}{n_f(n_f - 2n_c)}$$

Let us assume that $h''(n_f) \leq 0$ and derive a contradiction

$$\begin{aligned} \frac{2n_f \ln(n_f)}{(n_f - 2n_c)^3} - \frac{2(1 + \ln(n_f))}{(n_f - 2n_c)^2} + \frac{1}{n_f(n_f - 2n_c)} &\leq 0 \\ \frac{1}{2n_f} + \frac{n_f \ln(n_f)}{(n_f - 2n_c)^2} &\leq \frac{1 + \ln(n_f)}{n_f - 2n_c} \\ (n_f - 2n_c)^2 &\leq 2n_f(n_f - 2n_c)(1 + \ln(n_f)) - 2n_f^2 \ln(n_f) \\ 4n_c^2 + 4n_c n_f \ln(n_f) &\leq n_f^2 \end{aligned}$$

substitute n_c in terms of the critical n_f

$$\begin{aligned} n_c &= \frac{n_f}{2(1 + \ln(n_f))} \\ 4 \left(\frac{n_f}{2(1 + \ln(n_f))} \right)^2 + 4 \left(\frac{n_f}{2(1 + \ln(n_f))} \right) n_f \ln(n_f) &\leq n_f^2 \\ \frac{1}{(1 + \ln(n_f))^2} + \frac{2 \ln(n_f)}{1 + \ln(n_f)} &\leq 1 \\ 1 + 2(1 + \ln(n_f)) \ln(n_f) &\leq (1 + \ln(n_f))^2 \\ 1 + 2 \ln(n_f) + 2 \ln(n_f)^2 &\leq 1 + 2 \ln(n_f) + \ln(n_f)^2 \\ \ln(n_f)^2 &\leq 0 \\ n_f &\leq 1 \end{aligned}$$

The length of the FFT must be at least 3 if n_c is non-zero, and we have derived a contradiction, therefore, $h'(n_f) = 0 \Rightarrow h''(n_f) > 0$. \square

B. Table of variables used in text

Symbol	Description
c_h	The aggregate number of operations required for high memory mode
c_l	The aggregate number of operations required for low memory mode
c_e	The aggregate number of operations required for extremely low memory mode
m_h	The aggregate distributed memory requirement required for high memory mode
m_l	The aggregate distributed memory requirement required for low memory mode
m_e	The aggregate distributed memory requirement required for extremely low memory mode
m_{ns}	The per processor memory requirement for the noise filters in the stacked distribution mode
m_{nc}	The per processor memory requirement for the noise filters in the concatenated distribution mode
d_t	The per processor disk requirement for reading time stream of data
d_{ps}	The per processor disk requirement for reading compressed pointing in the stacked distribution mode
d_{pc}	The per processor disk requirement for reading compressed pointing in the concatenated distribution mode
d_{pd}	The per processor disk requirement for reading detector pointing without compressed pointing
d_{ns}	The per processor disk requirement for reading noise filters in the stacked distribution
d_{nc}	The per processor disk requirement for reading noise filters in the concatenated distribution
n_z	The number of pixels in the map
n_d	The number of detectors.
r_d	The detector sample rate
Δt	The integral time over which the telescope observed data
n_t	The total number of samples measured by all detectors.
n_i	The number of iterations required to solve the PCG
n_c	The correlation length of the noise
n_b	The number of stationary periods
r_p	The telescope telemetry data sample rate
n_{nz}	The number of non-zero elements per row of the pointing matrix.
n_{proc}	The number of processors used in a run.

Table 2: Some notes on the variables: The number of pixels in the map, n_z , is more generally the number of free parameters in the signal model which could include signals in addition to the pixels in the map and may include multiple maps. Note that for detectors sampled simultaneously and at the same rate $n_t = n_d r_d \Delta t$. The number of iterations required to solve the PCG, n_i is proportional to the condition number of the pixel-pixel noise correlation matrix after preconditioning. The correlation length of the noise, n_c , is also the band width of the diagonal blocks of the inverse time-time noise correlation matrix. The number of stationary periods, n_b , corresponds to the number of diagonal blocks in the inverse time-time noise correlation matrix. The telescope telemetry data sample rate, r_p , is more generally the minimum sample rate required to accurately reconstruct the pointing matrix A .

REFERENCES

- Armitage, C., & Wandelt, B. D. 2004, *Phys. Rev. D*, 70, 123007
- Armitage-Caplan, C., & Wandelt, B. D. 2008, ArXiv e-prints
- Ashdown, M. A. J., et al. 2007a, *A&A*, 471, 361
- . 2007b, *A&A*, 467, 761
- . 2009, *A&A*, 493, 753
- Barrett, R., et al. 1994, *Templates for the Solution of Linear Systems: Building Blocks for Iterative Methods*, 2nd Edition (Philadelphia, PA: SIAM)
- Bock, J., et al. 2006, ArXiv Astrophysics e-prints
- Borrill, J. 1999, ArXiv Astrophysics e-prints
- Brakhage, H. 1996, *SIAM Review*, 38, 682
- Burigana, C., & Sáez, D. 2003, *A&A*, 409, 423
- Cooley, J. W., & Tukey, J. W. 1965, *Journal of Mathematical Computations*, 19, 297
- de Bernardis, P., et al. 2000, *Nature*, 404, 955
- de Gasperis, G., Balbi, A., Cabella, P., Natoli, P., & Vittorio, N. 2005, *A&A*, 436, 1159
- Delabrouille, J. 1998, *A&AS*, 127, 555
- Dodelson, S. 2003, *Modern Cosmology* (525 B Street, Suite 1900, San Diego, California 92101-4495, USA: Academic Press)
- Doré, O., Teyssier, R., Bouchet, F. R., Vibert, D., & Prunet, S. 2001, *A&A*, 374, 358
- Frigo, M., & Johnson, S. G. 2005, *Proceedings of the IEEE*, 93, 216, special issue on "Program Generation, Optimization, and Platform Adaptation"
- Golub, G. H., & van Loan, C. F. 1996, *Matrix computations* (Johns Hopkins University Press)
- Górski, K. M., Hivon, E., Banday, A. J., Wandelt, B. D., Hansen, F. K., Reinecke, M., & Bartelmann, M. 2005, *ApJ*, 622, 759
- Grainger, W., et al. 2008, in *Society of Photo-Optical Instrumentation Engineers (SPIE) Conference Series*, Vol. 7020, Society of Photo-Optical Instrumentation Engineers (SPIE) Conference Series
- Hanany, S., et al. 2000, *ApJ*, 545, L5
- Hinshaw, G., et al. 2003, *ApJS*, 148, 135
- Janssen, M. A., et al. 1996, ArXiv Astrophysics e-prints
- Jewell, J., Levin, S., & Anderson, C. H. 2004, *ApJ*, 609, 1
- Johnson, B. R., et al. 2007, *ApJ*, 665, 42
- Keihänen, E., Kurki-Suonio, H., & Poutanen, T. 2005, *MNRAS*, 360, 390
- Keihänen, E., Kurki-Suonio, H., Poutanen, T., Maino, D., & Burigana, C. 2004, *A&A*, 428, 287
- Kuo, C. L., et al. 2004, *ApJ*, 600, 32
- Kurki-Suonio, H., Keihänen, E., Keskitalo, R., Poutanen, T., Sirvio, A., Maino, D., & Burigana, C. 2009, ArXiv e-prints
- Maino, D., et al. 1999, *A&AS*, 140, 383
- Oh, S. P., Spergel, D. N., & Hinshaw, G. 1999, *ApJ*, 510, 551
- Oxley, P., et al. 2004, in *Society of Photo-Optical Instrumentation Engineers (SPIE) Conference Series*, Vol. 5543, Society of Photo-Optical Instrumentation Engineers (SPIE) Conference Series, ed. M. Strojnik, 320–331
- Patanchon, G., et al. 2008, *ApJ*, 681, 708
- Poutanen, T., et al. 2006, *A&A*, 449, 1311
- Press, W., Teukolsky, S., Vetterling, W., & Flannery, B. 1992, *Numerical Recipes in C*, 2nd edn. (Cambridge, UK: Cambridge University Press)
- Reinecke, M., Dolag, K., Hell, R., Bartelmann, M., & Enßlin, T. A. 2006, *A&A*, 445, 373
- Shewchuk, J. R. 1994, privately on web
- Stompor, R., et al. 2002, *Phys. Rev. D*, 65, 022003

- Stompor, R., Leach, S., Stivoli, F., & Baccigalupi, C. 2009, MNRAS, 392, 216
- Stompor, R., & White, M. 2004, A&A, 419, 783
- Sutton, D., Johnson, B. R., Brown, M. L., Cabella, P., Ferreira, P. G., & Smith, K. M. 2009, MNRAS, 101
- Tegmark, M. 1997, Phys. Rev. D, 56, 4514
- The Planck Collaboration. 2005, ESA-SCI, ESA publications, 1
- Wandelt, B. D., Larson, D. L., & Lakshminarayanan, A. 2004, Phys. Rev. D, 70, 083511
- Waskett, T. J., Sibthorpe, B., Griffin, M. J., & Chanial, P. F. 2007, MNRAS, 381, 1583
- Wright, E. L., Hinshaw, G., & Bennett, C. L. 1996, ApJ, 458, L53+